Emergence of strong tunable linear Rashba spin-orbit coupling in two-dimensional hole gases in semiconductor quantum wells

Jia-Xin Xiong,[1,2] Shan Guan,[1,*] Jun-Wei Luo,[1,2,3,†] and Shu-Shen Li[1,2]

[1]*State Key Laboratory of Superlattices and Microstructures, Institute of Semiconductors, Chinese Academy of Sciences, Beijing 100083, China*

[2]*Center of Materials Science and Optoelectronics Engineering, University of Chinese Academy of Sciences, Beijing 100049, China*

[3]*Beijing Academy of Quantum Information Sciences, Beijing 100193, China*

(Received 24 August 2020; revised 28 December 2020; accepted 8 February 2021; published 23 February 2021)

Two-dimensional hole gases (2DHGs) in semiconductor quantum wells are promising platforms for spintronics and quantum computation, but suffer from the lack of the **k**-linear term in the Rashba spin-orbit coupling (SOC), which is essential for spin manipulations without magnetism. The Rashba SOC in 2DHGs is commonly believed to be a **k**-cubic term as the lowest order. Here, contrary to conventional wisdom, we taking Ge/Si system as an example uncover a strong and tunable **k**-linear Rashba SOC in 2DHGs of semiconductor quantum wells (QWs) by performing atomistic pseudopotential calculations in conjunction with theoretical analysis based on the effective model Hamiltonian approach. We illustrate that this emergent **k**-linear Rashba SOC is a first-order direct Rashba effect, originating from a combination of heavy-hole-light-hole mixing and direct dipolar coupling to the external electric field. The enhanced interband mixing renders [110]-oriented Ge/Si QWs a much stronger linear Rashba SOC than [001]-oriented counterpart with the maximal strength exceeding 120 meVÅ, comparable to the highest values reported in two-dimensional electron gases made by narrow band-gap III-V semiconductors, which suffers from short spin lifetime due to the presence of nuclear spin. These findings confirm Ge-based 2DHGs to be an excellent platform for large-scale quantum computation.

DOI: 10.1103/PhysRevB.103.085309

I. INTRODUCTION

Spin-orbit coupling (SOC) entangles the spin and orbital degrees of freedom and has inspired a vast number of predictions, discoveries, and innovative concepts, including spin transistors, spin-orbit qubits, spin Hall effect, quantum spin Hall effect, topological insulators, and Majorana fermions [1–12]. The exploration, understanding, and control of SOC have become intensive research subjects across many different disciplines in condensed matter physics. Very recently, the strong Rashba SOC of holes in the platform of Ge quantum wells (QWs) has been demonstrated to provide an efficient driving manner for rapid qubit control [13]. The electric-field tunability of the Rashba SOC further ensures the independent control of multiple qubits [13]. In contrast, the absence of strong SOC in Si demands the inclusion of complicated components in the proximity of each qubit to control the qubit. It leads the scalability of Si qubits to be a key challenge [13], despite the fact that Si qubits so far have been considered as the most promising platform for large-scale quantum computation [9,13]. Since holes are free from the challenge of valley degeneracy, and Ge has the highest hole mobility among all known semiconductors, reaching a hole mobility over 1.5 million $cm^2/(V \cdot s)$ at 3 K in strained Ge QWs [14], strong SOC of holes renders Ge QWs as the excellent platform for large-scale quantum computation.

However, the Rashba SOC of the ground hole subband in semiconductor QWs, including Ge QWs, is commonly believed to be **k**-cubic rather than **k**-linear as the lowest order [15–17] (see Appendix A for details). This is in sharp contrast to the electron counterpart, in which a variety of potential applications was proposed based on the **k**-linear term. We schematically illustrate the different features between the **k**-cubic and **k**-linear Rashba SOC in Fig. 1. First, compared to the **k**-linear spin splitting, the **k**-cubic spin splitting is negligible for light doping semiconductors due to their rather small Fermi wave vector k_F, which is close to the $\bar{\Gamma}$ point. Thus, from the perspective of spin splitting, the **k**-linear or **k**-cubic Rashba SOC is a "yes-or-no" question rather than a "large-or-small" question for many applications. Second, as indicated in Figs. 1(b) and 1(c), the texture of the Rashba SOC induced effective magnetic field in the momentum space is completely different for **k**-linear and **k**-cubic terms. Considering the substantively different rotation rates, only the effective magnetic field of the **k**-linear Rashba SOC is able to be affectively "locked" perpendicular to the momentum, providing more precise control over the spin direction. Third, in real space, as shown in Figs. 1(b) and 1(c), the **k**-linear Rashba SOC induces a much faster spin precession than the **k**-cubic Rashba SOC, leading to a reduction of two orders of magnitude smaller in the smallest device length. This advantage of the **k**-linear Rashba SOC makes a possibility for developing ultra-small hole spin transistors.

Because of these compelling differences between **k**-linear and **k**-cubic terms, the lack of strong **k**-linear Rashba SOC excludes holes in QWs from many potential applications. Luo

*shan_guan@semi.ac.cn
†jwluo@semi.ac.cn

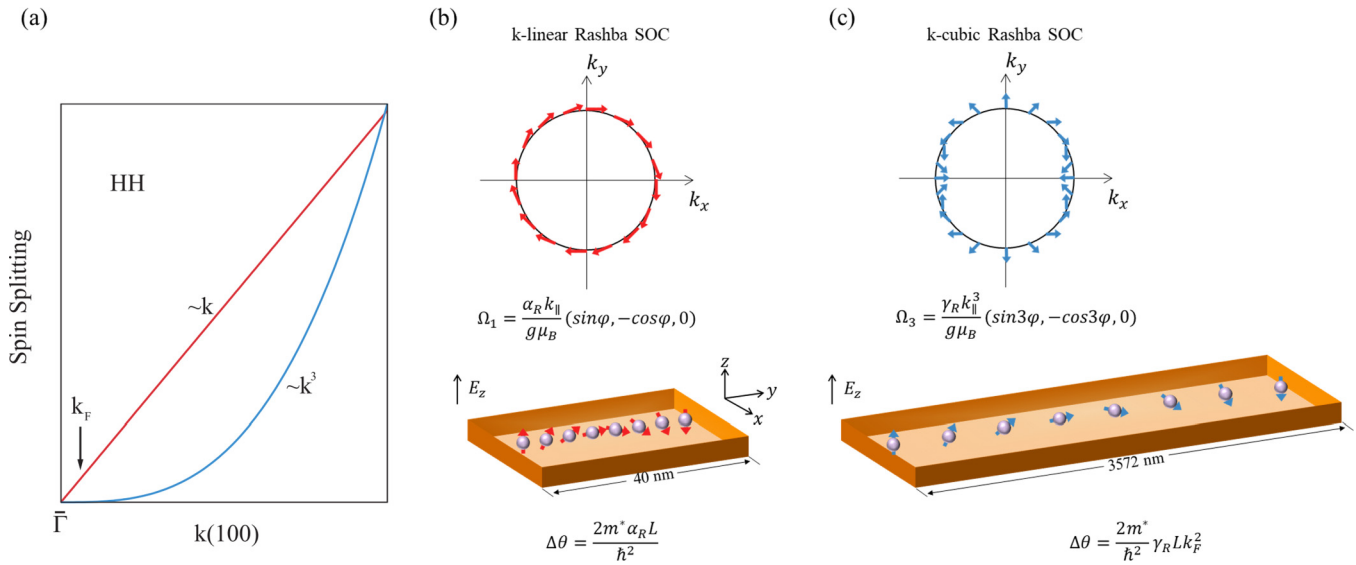

FIG. 1. Schematical illustration of the compelling different features between **k**-linear (marked in red) and **k**-cubic (marked in blue) Rashba SOC. (a) Rashba spin splitting of the ground heavy hole (HH) subband around $\bar{\Gamma}$ point in semiconductor quantum wells. The effective magnetic field texture of (b) **k**-linear and (c) **k**-cubic Rashba SOC in the momentum space and the corresponding spin precession $\Delta\theta$ in the real space. Here α_R (γ_R) is the **k**-linear (**k**-cubic) Rashba parameter, Ω_1 (Ω_3) the **k**-linear (**k**-cubic) effective magnetic field, φ the angle between spin orientation and k_x direction, k_F the Fermi wave vector, L the spin precession length of hole spin transistors, m^* the hole effective mass (we take $0.3m_0$ for Ge, where m_0 is the mass of bare electron). The expressions of the spin precession angle based on the **k**-linear and **k**-cubic Rashba SOC are given in Refs. [1,18], respectively. For the **k**-cubic SOC with a Rashba parameter $\gamma_R = 2.26 \times 10^5$ meV Å^3 (value adopted from Ref. [19] for Ge) and the Fermi wave vector is $0.002 \times 2\pi/a$ ($a = 5.65$ Å is the lattice constant of Ge), the spin precession length will be 3.6 μm. However, for the **k**-linear SOC with a Rashba parameter $\alpha_R = 100$ meVÅ (value within the range of our SEPM results), the spin precession length will be 40 nm, which is two orders of magnitude smaller than the length of the **k**-cubic Rashba SOC.

et al. [20] and Kloeffel *et al.* [21] independently found, in one-dimensional (1D) quantum wires, the emergence of a strong **k**-linear hole Rashba SOC, originating from a direct dipolar coupling between heavy-hole (HH) and light-hole (LH) subbands by an external electric field [21–23]. Such a giant **k**-linear Rashba effect, called the direct Rashba effect, is a first-order effect and much stronger than the conventional third-order Rashba effect. The strength of the direct Rashba SOC scales with the HH-LH coupling at zone center ($\bar{\mathbf{k}} = 0$) and is thus supposed to vanish in two-dimensional (2D) QWs in which the HH-LH coupling is commonly considered to be forbidden by symmetry [15]. However, both experiments and numerical simulations have demonstrated finite zone-center HH-LH coupling in QWs [24–30]. One hence expects that a strong **k**-linear hole direct Rashba SOC may also exist in QWs. Such an expectation is highly relevant to the current understanding of 2D hole spin physics, such as spin-Hall conductivity [7,31–34], spin-galvanic effect [35], hole spin helix [36], and current-induced spin polarization [37] since all these effects were investigated based on the assumption of the **k**-cubic Rashba SOC [38].

In this article, we study the Rashba SOC via examining the spin splitting of energy bands in Ge/Si QWs using the atomistic semi-empirical pseudopotential method (SEPM) [39–41] in combination with the theoretical analysis based on the Luttinger-Kohn Hamiltonian. We indeed find a finite **k**-linear spin splitting in both [001]- and [110]-oriented Ge/Si QWs, induced by a direct Rashba SOC as comfirmed based on an effective Hamiltonian considering a finite HH-LH mixing. The stronger interband mixing results in [110]-oriented QWs having a much stronger linear Rashba SOC than [001]-oriented QWs. Our predicted Rashba parameter α_R in [110]-oriented Ge/Si QWs can be as large as 120 meVÅ, which is among the largest values measured in 2D electron systems made by narrow band-gap group III-V semiconductors [12]. This electric-field tunability of the 2D **k**-linear Rashba SOC over an extremely broad range of strength, covering more than two orders of magnitude, demonstrates its predominance over 2D **k**-linear Dresselhaus SOC [24], providing a promising platform for hole spin transistors.

This paper is organized as follows. In Sec. II, we present a computational method for SOC-included spin splitting. The results are shown in Sec. III, where we also perform the theoretical analysis based on an effective model Hamiltonian considering HH-LH mixing to explain the predicted **k**-linear Rashba SOC. We do a brief survey of potential applications of the **k**-linear Rashba effect in Sec. IV to further illustrate the importance of this effect. In Sec. V, we discuss the conventional **k**-cubic Rashba effect, which differs from the discovered direct Rashba effect in this work. Finally, we summarize our results in Sec. VI.

II. COMPUTATIONAL METHODS

Our calculations are based on a supercell approach with a periodic boundary condition. The supercell contains one Ge/Si QW with a unit cell of $1 \times 1 \times (m + n)$ atomic layers (m and n denote Ge and Si thickness in atomic layers). We find that 20 atomic layers of the Si barrier are thick enough to confine the holes in the Ge well. Since the difference in lattice

constants of bulk Si (5.4307 Å) and Ge (5.6579 Å) results in a 4.2% lattice mismatch, we use the valence force field (VFF) approach to minimize the strain energy occurred in Ge/Si QWs. The VFF approach has been successfully and widely applied to conventional semiconductors [42], including Si and Ge (see Appendix B for detailed parameters) [25,43–45]. The relaxed structures [46–48] of [001]- and [110]-oriented Ge_{40}/Si_{20} QWs show a 1% compressive strain occured in the Ge well and a 3% tensile strain in the Si barrier.

Electronic structures of QWs are then calculated using the atomistic semipseudopotential method (SEPM) accompanied with a plane-wave basis set and folded-spectrum diagonalization [39], which was extensively utilized to study semiconductor superstructures [20,23–25,46,47,49–51]. An energy cutoff of 8.2 Ry is used to select the plane-wave basis, and fast Fourier transformations are used to transform the wave function between a real space grid and a reciprocal space grid. A $16 \times 16 \times 16$ grid in real space is used for each eight-atom cubic (diamond or zinc-blende) cell [40,41]. The crystal potential of QWs is a superposition of screened atomic potentials, which contain a local part and a nonlocal spin-orbit interaction part of all atoms in the QWs. The construction of atomic potentials is the key to accuracy and realism and was obtained by fitting to reproduce experimental transition energies, effective masses, spin-orbit splittings, and deformation potentials of the bulk semiconductors to remove the "LDA error" [40,41]. The spin splitting energy is extracted from the calculated band structure, and the **k**-linear and **k**-cubic Rashba parameters are obtained by fitting the obtained spin splitting.

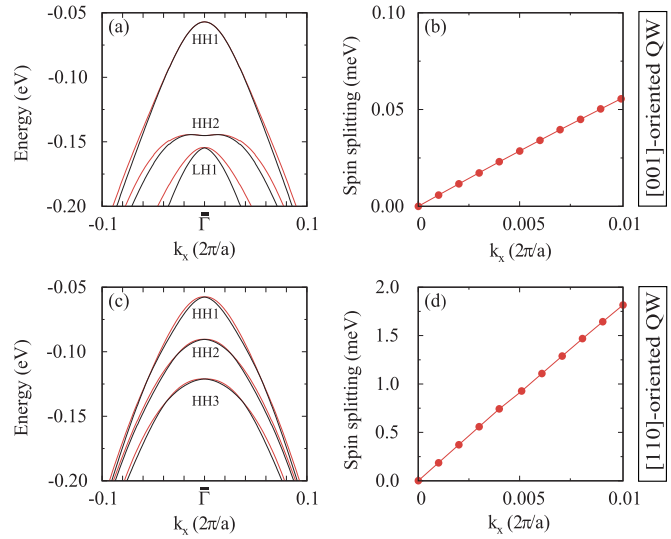

FIG. 2. Calculated energy dispersion of valence subbands and spin splitting of HH1 for (a, b) [001]-oriented $(Ge)_{40}/(Si)_{20}$ QW and (c, d) [110]-oriented $(Ge)_{40}/(Si)_{20}$ QW, respectively, under an electric field $E_z = 100$ kV/cm perpendicular to the interface. Here, the thickness (subscripts) units in monolayer (ML). The x-direction in [001]- and [110]-oriented QWs is along the crystalline [100] and [001] directions, respectively. The labels HH1, HH2, HH3, and LH1 indicate the valence subbands derived mainly from either bulk HH or LH bands. The label a denotes the lattice constant, which is 5.5792 Å and 5.5796 Å for [001]- and [110]-oriented $(Ge)_{40}/(Si)_{20}$ QWs, respectively, after VFF relaxation. The Ge-Ge bonding length is 2.4353 Å and 2.4380 Å for [001]- and [110]-oriented QWs, and the Si-Si bonding length is 2.3763 Å and 2.3673 Å for [001]- and [110]-oriented QWs, respectively.

III. RESULTS

A. k-linear Rashba spin splitting

Figures 2(a) and 2(c) show the SEPM calculated valence band structure of [001]- and [110]-oriented Ge/Si QWs upon application of an electric field of 100 kV/cm perpendicular to the QWs. The states of the conduction subbands are confined in Si layers while states of the valence subbands are confined in Ge layers (not shown) due to the valence band maximum (VBM) of bulk Ge being 0.5 eV higher than the bulk Si [15]. We find that the doubly spin-degenerate subbands split away from the $\bar{\Gamma}$ point giving rise to spin-splitting $\Delta E_{ss}(k_\parallel)$, which is shown in Figs. 2(b) and 2(d) for the ground-state subband derived from the bulk HH band (HH1). $\Delta E_{ss}(k_\parallel)$ exhibits a nice linear scale against the in-plane wave vector k_x. Due to the existence of an inversion center, the bulk inversion asymmetry-induced Dresselhaus spin splitting [52] is absent in Ge/Si QWs. Hence, the obtained spin splitting is completely induced by the Rashba effect [53]. Interestingly, we find that spin-splitting is isotropic in [001]-oriented QWs but anisotropic in [110]-oriented QWs [15]. This anisotropy is due to the breaking of the axial symmetry and will be explained below. To deduce the linear (α_R) and cubic (γ_R) Rashba parameters, we fit spin-splitting $\Delta E_{ss}(k_\parallel)$ of the HH1 subband to the equation $\Delta E_{ss}(k_\parallel) = 2\alpha_R k_\parallel + \gamma_R k_\parallel^3$, obtaining $\alpha_R = 3,82$ meVÅ for [001]- and [110]-oriented $(Ge)_{40}/(Si)_{20}$ QWs (under an external field of 100 kV/cm), respectively. The cubic parameters γ_R are found to be negligibly small (smaller than 1 meVÅ^3). The α_R value of [110]-oriented QWs is comparable to that of direct hole Rashba SOC predicted in 1D quantum wires [23].

We then turn to examine the field- and size-dependencies of the **k**-linear Rashba parameter α_R for both [001]- and [110]-oriented QWs. Figure 3(a) shows that α_R scales linearly against E_z for the [001]-oriented $(Ge)_{40}/(Si)_{20}$ QW, but sublinearly for the [110]-oriented $(Ge)_{40}/(Si)_{20}$ QW, in which the difference of α_R along k_x and k_y directions becomes more obvious with increasing E_z. Under a fixed electric field $E_z = 100$ kV/cm with varying well thickness, as shown in Fig. 3(b), α_R increases linearly against the well thickness for [001]-oriented QWs. Whereas, for [110]-oriented QWs, α_R increases linearly in a much larger rate in well thickness when $L < 20$ ML, and then grows slowly towards saturation. The difference of α_R along k_x and k_y directions is negligible when $L < 20$ ML and enlarges quickly with further increasing L. The field- and size-dependencies of α_R in [110]-oriented QWs are similar to the case of 1D quantum wires [23], indicating spin-splitting arising from the first-order direct Rashba SOC rather than conventional third-order Rashba SOC. Interestingly, $\alpha_R^{[110]}$ is one order of magnitude larger than $\alpha_R^{[001]}$, and is strongly tunable by external field to exceed 120 meVÅ. This strong tunable Rashba SOC in [110]-oriented QWs is a striking property for hole spin manipulation.

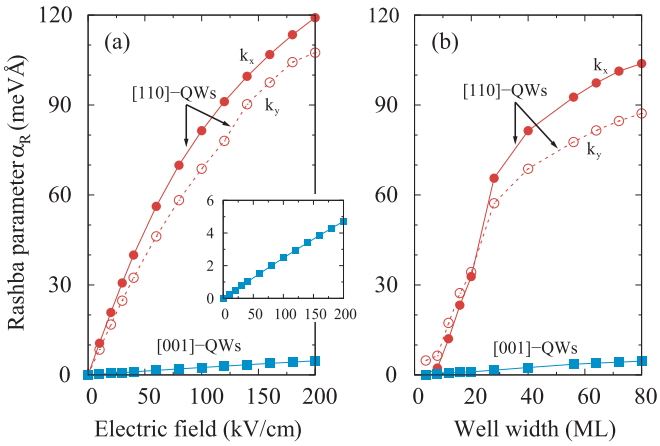

FIG. 3. Calculated **k**-linear hole Rashba parameters α_R in Ge/Si QWs as a function of (a) electric field strength with 40 ML well thickness, and (b) well thickness under an electric field of 100 kV/cm, respectively. The Si thickness is 20 ML. For [110]-oriented QWs, the x- and y-directions are along the crystalline [001] and [1$\bar{1}$0] directions, respectively. The inset to (a) shows a linear dependence in [001]-oriented QWs, reflecting the negligible QCSE in comparison to QCE. Note that a larger electric field strength than 200 kV/cm is not experimentally available, hence the results are not shown.

B. Origin of the k-linear Rashba SOC

We turn to unravel the origin of the emergence of **k**-linear hole Rashba SOC and illustrate the decisive role of the HH-LH mixing through the envelope function approximation based on the Luttinger-Kohn (LK) Hamiltonian. The lowest-energy subband spectrum is governed by the effective Hamiltonian projected into the subspace spanned by the four states $|\mathrm{HH1}_\pm\rangle$ and $|\mathrm{HH2}_\pm\rangle$ of the two topmost HH-like subbands (indicated in the SEPM band structure by HH1 and HH2) at the $\bar{\Gamma}$-point. The four basis states are constructed by including the HH-LH mixing: $|\mathrm{HH1}_\pm\rangle = a_1\phi_1(z)|\frac{3}{2},\pm\frac{3}{2}\rangle + b_1\phi_1(z)|\frac{3}{2},\mp\frac{1}{2}\rangle$ and $|\mathrm{HH2}_\pm\rangle = a_2\phi_2(z)|\frac{3}{2},\pm\frac{3}{2}\rangle + b_2\phi_2(z)|\frac{3}{2},\mp\frac{1}{2}\rangle$, where a_1 and b_1 (a_2 and b_2) are real coefficients of bulk HH and LH Bloch functions in QW HH1 (HH2) states, respectively, and envelope functions $\phi_n(z) = \sqrt{\frac{2}{L}}\sin[\frac{n\pi(z+L/2)}{L}]$, $n \in \{1,2,\ldots\}$, by assuming an infinite confinement potential.

In the [001]-oriented QWs with D_{2d} symmetry, the HH-LH mixing at $\bar{\mathbf{k}} = 0$ originates from symmetry reduction caused by the local symmetry of the C_{2v} interface [25,26], otherwise is absent (i.e., $b_{1,2} = 0$). Starting from the [001]-oriented three-dimensional (3D) LK Hamiltonian [21,54], we obtain the 4×4 effective Hamiltonian of 2D [001]-oriented QWs in the absence of the external electric field

$$H_{\mathrm{eff}}^{[001]} = A_+ + A_-\tau_z + \gamma_3 C_0 \tau_x(k_x\sigma_y - k_y\sigma_x), \qquad (1)$$

where τ and σ are the Pauli matrices describing the orbital part and the spin part of the eigenstates, respectively, and γ_3 is the LK parameter. $A_\pm = \hbar^2k_x^2(m_{1x}^{-1} \pm m_{2x}^{-1})/4 + \hbar^2k_y^2(m_{1y}^{-1} \pm m_{2y}^{-1})/4 \pm \Delta_0/2$, where m_{1x} and m_{1y} (m_{2x} and m_{2y}) are effective masses along x- and y-directions, respectively, for the HH1 (HH2) subband and Δ_0 is the energy separation between HH1 and HH2 states arising from the space confinement effect (SCE). The off-diagonal term $\langle \mathrm{HH1}_\pm|H_{\mathrm{eff}}^{[001]}|\mathrm{HH2}_\mp\rangle = \mp i\gamma_3 C_0(k_x \mp ik_y)$, where the coupling parameter $C_0 = (a_1b_2 - a_2b_1)\frac{8\sqrt{3}\hbar^2}{3m_0L}$ reflects the strength of HH-LH mixing.

Upon application of an external electric field E_z to [001]-oriented QWs, E_z will couple directly to the spins owing to HH-LH mixed QW states, yielding a direct dipolar coupling term $\langle \mathrm{HH1}_\pm|(-eE_zz)|\mathrm{HH2}_\pm\rangle = eE_zU_0$, where the coupling constant $U_0 = (a_1a_2 + b_1b_2)\frac{16L}{9\pi^2}$ is also related to the HH-LH mixing. Using the quasidegenerate perturbation theory [55], we finally obtain the first-order 2×2 effective Rashba SOC Hamiltonian for the HH1 subband: $H_{\mathrm{soc}}^{[001]} = \alpha_R^{[001]}(k_x\sigma_y - k_y\sigma_x)$ (see Appendix C for details), where the **k**-linear Rashba parameter reads

$$\alpha_R^{[001]} = \frac{2e\gamma_3C_0U_0E_z}{\sqrt{\Delta_0^2 + 4e^2U_0^2E_z^2}}. \qquad (2)$$

The denominator term is the energy separation $\Delta E_{1,2}$ between HH1 and HH2 induced by SCE (Δ_0) and quantum-confined Stark effect (QCSE) ($2eU_0E_z$). We clearly observe that $\alpha_R^{[001]}$ scales linearly with E_z when $2eU_0E_z \ll \Delta_0$, in excellent agreement with the SEPM results shown in Fig. 3(a). The **k**-linear Rashba SOC originates from a combination of the HH-LH mixing and the direct dipolar coupling to the external electric field, with $\alpha_R^{[001]}$ having the same formula [Eq. (2)] as that of the direct Rashba SOC in 1D nanowires [21]. Hence, the **k**-linear Rashba SOC uncovered in [001]-oriented QWs is a 2D direct Rashba effect.

In the [110]-oriented QWs, in addition to the interface-induced HH-LH mixing, the breaking of the axial symmetry causes an intrinsic HH-LH mixing at $\bar{\mathbf{k}} = 0$ [15] with its magnitude proportional to $(\gamma_3 - \gamma_2) \times \hat{k}_z^2$, where $\hat{k}_z^2 \sim (\pi/L)^2$ [22]. This intrinsic HH-LH mixing leads to an enhanced direct Rashba effect in [110]-oriented QWs in comparison to [001]-oriented QWs as we observed in the SEPM results (Fig. 3). We perform the same procedure as done in [001]-oriented QWs and obtain an in-plane anisotropic linear Rashba SOC (see Appendix D for details)

$$\alpha_R^{[110]}(k_x) = \frac{2e\gamma_3C_0U_0E_z}{\sqrt{{\Delta_0}^2 + 4e^2{U_0}^2E_z^2}}, \qquad (3)$$

and

$$\alpha_R^{[110]}(k_y) = \frac{2e\gamma_2C_0U_0E_z}{\sqrt{{\Delta_0}^2 + 4e^2{U_0}^2E_z^2}}. \qquad (4)$$

We find $\alpha_R^{[110]}(k_x)/\alpha_R^{[110]}(k_y) \approx \gamma_3/\gamma_2$ [the Luttinger parameters for Ge are $\gamma_3 = 5.69$ and $\gamma_2 = 4.24$ [38], hence $\alpha_R^{[110]}(k_x)/\alpha_R^{[110]}(k_y) \approx 1.34$], which explains the SEPM results shown in Fig. 3.

C. Reason of much larger Rashba SOC in [110]-oriented Ge/Si QWs

To understand the observed differences between [001]- and [110]-oriented QWs in the field- and size-dependencies of Rashba SOC strength (α_R as shown in Fig. 3), we next turn to examine the energy separation $\Delta E_{1,2}$ which is the denominator term in the expression of Rashba parameters [Eqs. (2)

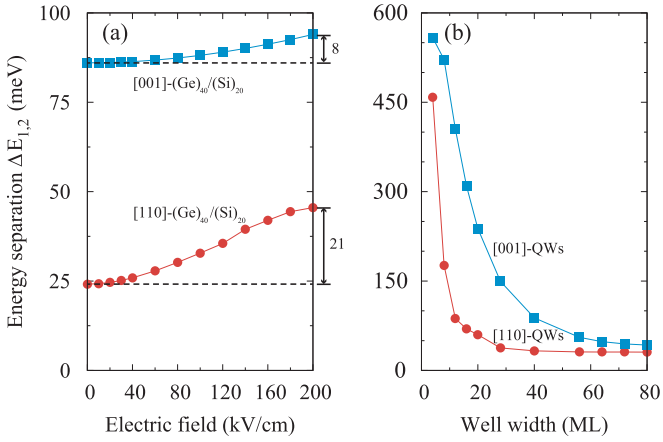

FIG. 4. Energy separation $\Delta E_{1,2} = \sqrt{\Delta_0^2 + 4e^2U_0^2E_z^2}$ between HH1 and HH2 states at Γ point in [001]- and [110]-oriented Ge/Si QWs as a function of (a) electric field strength for a fixed QW thickness and (b) well thickness with an applied electric field of 100 kV/cm, respectively.

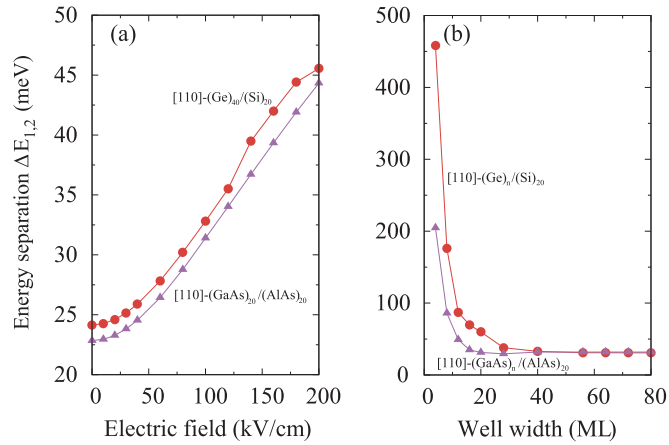

FIG. 5. Energy separation $\Delta E_{1,2} = \sqrt{\Delta_0^2 + 4e^2U_0^2E_z^2}$ between HH1 and HH2 states at Γ point in [110]-oriented GaAs/AlAs QWs and [110]-oriented Ge/Si QWs as a function of (a) electric field for fixed well thickness and of (b) well thickness with applied 100 kV/cm electric field, respectively.

to (4)]. Figure 4(a) shows $\Delta E_{1,2}$ as a function of the applied electric field E_z for a fixed thickness $L = 40$ ML, in which $\Delta E_{1,2}$ is solely induced by SCE at $E_z = 0$. With increasing E_z, $\Delta E_{1,2}$ grows in substantially different rates for [001]- and [110]-oriented QWs. A much larger rate in [110]-oriented QWs implies a stronger QCSE, illustrating that the HH-LH mixing and the direct Rashba SOC could strongly respond to the external electric field. At $E_z = 200$ kV/cm, we find that the QCSE contributes 50% to $\Delta E_{1,2}$ in [110]-oriented QWs, but less than 10% in [001]-oriented QWs. The significantly enhanced contribution of QCSE ($2eU_0E_z$) to $\Delta E_{1,2}$ causes a sublinear field dependence of α_R as observed in [110]-oriented QWs [Eq. (3) and Fig. 3(a)]. Whereas, in [001]-oriented QWs, the weak field dependence of $\Delta E_{1,2}$, implying a much weaker QCSE, leads to a linear scale of α_R as applied field E_z [Eq. (2) and Fig. 3(a)]. Figure 4(b) displays $\Delta E_{1,2}$ against the well thickness L under a fixed E_z. We see that, with increasing L, $\Delta E_{1,2}$ drops rapidly for $L \leqslant 40$ ML and then decreases slowly towards the bulk zero value owing to the reduced SCE. Interestingly, in addition to the much stronger QCSE, [110]-oriented QWs have a three to four times smaller $\Delta E_{1,2}$ than [001]-oriented QWs. In combination with the enhanced HH-LH mixing originated from the breaking of the axial symmetry, [110]-oriented QWs possess an order stronger **k**-linear Rashba SOC than [001]-oriented QWs.

We note that the **k**-linear Rashba SOC is also applicable to two-dimensional hole gases (2DHGs) in other tetrahedral semiconductors, such as GaAs/AlAs QWs (see Appendix E for details). For III-V group semiconductors with zinc-blende structure, the [110]-oriented QWs have C_{2v} symmetry along the [001] crystalline direction, resulting in no Dresselhaus spin-splitting in this direction [20] and the spin-splitting is completely induced by the Rashba effect. We find that the Rashba parameters of GaAs/AlAs QWs are approximately half as large as Ge/Si QWs (see Appendix E), but their energy separations are close to each other (Fig. 5). Using the effective model, we mainly attribute these results to the different material-dependent LK parameter γ_3, where $\gamma_3(\text{Ge}) = 5.69$ is about twice as large as $\gamma_3(\text{GaAs}) = 2.90$ [15]. The results of GaAs/AlAs QWs further improve the reliability of the effective model and also extend the **k**-linear Rashba SOC into III-V group semiconductor QWs.

IV. POTENTIAL APPLICATIONS OF THE k-LINEAR RASHBA EFFECT

The **k**-linear Rashba effect plays a significant role in 2D electron systems. However, the absence of this **k**-linear term in 2D hole systems rules out its potential applications. Our results will force us to review all the effects related to hole spins in 2D systems, further driving forward the development of devices. Table I summarizes the potential applications of this **k**-linear term, whereby we also list the formulas connecting the concerning physical quantities and the **k**-linear Rashba parameter to show the impact of the **k**-linear term more clearly. For example, the interplay between the linear Rashba and Dresselhaus effect with equal strength, i.e., $\alpha_R = \pm\beta_D$, guarantees the spin precession robust against spin scatterings in [001]-oriented QWs, leading to a long spin lifetime [2,56]. This property, protected by SU(2) symmetry [58], is crucial to devices such as nonballistic spin-field-effect transistors [2]. The past point of view that only the **k**-cubic Rashba effect exists in 2D hole systems overlooks this **k**-linear counterpart, thus misleading us ruling out the 2D hole systems for high-quality spin transport. This emergence of the **k**-linear Rashba spin splitting fills this void. The effects related to the **k**-linear Rashba spin splitting, where electrons have in 2D systems, become implementable for holes at present.

However, the **k**-linear Rashba effect for holes is not the reprint of electrons. Although both electrons and holes have the effective Hamiltonian in the same form, they possess different effective spins because of the different orbital angular momentums. One example is the intrinsic spin Hall effect, which converts the unpolarized charge current to chargeless pure spin current (Table I) [5,7]. The spin Hall conductivity will have a different expression due to the change in

TABLE I. Physical effects related to spin-orbit interaction and their applications [12]. Here, α_R and γ_R denote **k**-linear and k-cubic Rashba parameters, respectively. β_D represents the **k**-linear Dresselhaus parameter. e is the elementary charge, $\hbar$ the reduced Plank constant, m^* the effective mass. $\vec{\sigma}$ is the Pauli matrix, $\vec{p}$ the momentum.

Phenomenon	Physical quantity	Formula	Application
Spin relaxation suppression [56]	Spin relaxation time $\tau_\pm$, **k**-linear Rashba parameter α_R, Dresselhaus parameter β_D	$\frac{1}{\tau_\pm} \propto (\alpha_R \pm \beta_D)^2$	Nonballistic spin-field-effect transistors [2]
Spin Hall effect (SHE) [5,7]	Spin Hall conductivity σ_H, spin current $\hat{j}^z_{\text{spin}}$, hole velocity $\vec{v}$	$\sigma_H = \frac{e\hbar}{V}\Sigma_{k,n\neq n'}(f_{n',k} - f_{n,k}) \times \frac{Im[\langle n'k\vert\hat{j}^z_{\text{spin},x}\vert nk\rangle\langle nk\vert v_y\vert n'k\rangle]}{(E_{nk}-E_{n'k})(E_{nk}-E_{n'k}-\hbar\omega-i\eta)}$	All-semiconductor spin Hall effect transistor [57]
Spin-galvanic effect [60,61]	Induced charge current density $\vec{j}_c$, non-equilibrium spin density $\vec{S}$	$\vec{j}_c = -e\alpha_R\frac{\hat{z}\times\vec{S}}{\hbar}$	Non-local spin detection [59]

expression of spin current and hole velocity. Another example is the spin galvanic effect, where nonequilibrium spin density created by optical or electrical means is converted to a charge current (Table I) [59–61]. Both the induced charge current density $\vec{j}_c$ and the nonequilibrium spin density $\vec{S}$ are associated with the effective spins.

V. DISCUSSION

Even in the absence of the direct dipolar coupling, Winkler [15] argued that the HH-LH mixing at $\bar{\mathbf{k}} = 0$ will also produce a conventional **k**-linear Rashba term to HH-like subbands. However, this conventional **k**-linear Rashba SOC effect is small compared to the **k**-cubic term. Kloeffel [21] demonstrated that, in 1D nanowires, this conventional **k**-linear Rashba SOC is in the third order of multiband perturbation theory and hence different from the first-order direct Rashba SOC in both field and size dependence. Specifically, the conventional **k**-linear Rashba term is 10 to 100 times weaker than the direct Rashba SOC, and is stronger in narrower QWs, which is opposite to the results shown in Fig. 3. We note that in a recent experiment the **k**-linear Rashba SOC of the 2DHG is claimed to be absent in [001]-oriented strained Ge/SiGe QWs, where the weak antilocalization (WAL) feature in the magnetoconductivity measurement failed to be described by the **k**-linear term alone but described well by the **k**-cubic term alone [19]. First, we have to stress that both **k**-linear and **k**-cubic terms are presented in the SEPM results, although the **k**-linear term dominates over the **k**-cubic term in an extreme small **k**-range. Therefore, in fitting to WAL data, one has to include both **k**-linear and **k**-cubic terms instead of exclusively considering the **k**-linear or **k**-cubic term only [19]. Second, the experiment adopts different barrier materials (SiGe alloy) from our barrier (Si). Adopting the SiGe alloy can reduce the lattice mismatch, and may induce the breaking of inversion symmetry, giving rise to Dresselhaus spin-splitting. Third, the experiment was conducted at the temperature range of 1.6 to 10 K, while the SEPM results give an order of tens μeV spin splitting in the [001]-oriented QWs, corresponding to a temperature lower than 1 K. Therefore, the temperature is still too high to observe this **k**-linear effect in the experiment. By contrast, the much larger Rashba spin splitting in [110]-oriented QWs may facilitate further experimental characterization.

We next clarify the feasibility of the growth of [110]-oriented Ge/Si QWs in experiments. In general, most Ge/SiGe QWs are fabricated along the [001] direction (usually adopting the SiGe alloy to eliminate the lattice mismatch induced built-in strain) [62,63]. Growth along the [111] direction was recently demonstrated [64]. We also find a series of literature that reported the growth of Si/SiGe or SiGe/Si QWs along the [110] direction [65–70], although more literature reported the growth of Ge-on-insulator p-channel metal-oxide-semiconductor-field-effect-transistors (MOSFETs) [71] and Ge layers on Si(110) substrates [72]. Our current finding may stimulate research efforts to grow [110]-oriented Ge/SiGe QWs.

VI. CONCLUSION

In conclusion, we uncover a strong electric-tunable **k**-linear Rashba SOC of 2DHGs in Ge/Si QWs. We illustrate that this previous unknown **k**-linear Rashba SOC is a first-order direct Rashba effect, originating from a combination of HH-LH mixing and direct dipolar intersubband coupling. Specifically, in [110]-oriented Ge/Si QWs, the strength of this **k**-linear Rashba SOC can be significantly enhanced by applied electric field to exceed 120 meVÅ, comparable to the largest values of 2D electron gases reported in narrow band gap III-V semiconductors, facilitating the fast manipulation of hole spins. This finding renders 2DHGs in Ge/Si QWs an excellent platform for quantum computation. These results make a call to revisit the understanding of 2D hole spin physics, which were explored with the assumption of **k**-cubic Rashba SOC.

ACKNOWLEDGMENTS

The authors thank Professor X. W. Zhang for helpful discussion. The work was supported by the National Science Fund for Distinguished Young Scholars under Grant No. 11925407, the Basic Science Center Program of the National Natural Science Foundation of China (NSFC) under Grant No. 61888102, and the Key Research Program of Frontier Sciences, CAS under Grant No. ZDBS-LY-JSC019. S. G. was also supported by the NSFC under Grant No. 11904359.

APPENDIX A: 2D k · p MODEL HAMILTONIAN

According to the bulk symmetry, the Hamiltonian describing HH and LH states is [73]

$$H_{SO} = \beta_1 \mathbf{k} \times \mathbf{E} \cdot \mathbf{J} + \beta_2 \mathbf{k} \times \mathbf{E} \cdot \mathcal{J}, \tag{A1}$$

TABLE II. Bond-length parameters of Ge and Si. Here, α, α_3, and α_4 are the bond stretching parameters.

Types	Bond length (Å)	α	α_3	α_4
Si-Si	2.351562	49.9995	−154.88	540.13
Ge-Ge	2.449943	33.1495	−128.58	260.25
Ge-Si	2.400753	41.5745	−150.38	381.62

where $\mathbf{J} = (J_x, J_y, J_z)$ and $\mathcal{J} = (J_x^3, J_y^3, J_z^3)$, with J_x, J_y, J_z are the angular momentum matrices for $j = 3/2$. For QWs confined in the z-direction, where the external electric field is applied, Eq. (A1) can be written as

$$H_{SO} = \beta_1 E_z \begin{pmatrix} 0 & 0 & i\frac{\sqrt{3}}{2}k_- & 0 \\ 0 & 0 & 0 & -i\frac{\sqrt{3}}{2}k_+ \\ -i\frac{\sqrt{3}}{2}k_+ & 0 & 0 & ik_- \\ 0 & i\frac{\sqrt{3}}{2}k_- & -ik_+ & 0 \end{pmatrix} + \beta_2 E_z \begin{pmatrix} 0 & -i\frac{3}{4}k_+ & i\frac{7\sqrt{3}}{8}k_- & 0 \\ i\frac{3}{4}k_- & 0 & 0 & -i\frac{7\sqrt{3}}{8}k_+ \\ -i\frac{7\sqrt{3}}{8}k_+ & 0 & 0 & i\frac{5}{2}k_- \\ 0 & i\frac{7\sqrt{3}}{8}k_- & -i\frac{5}{2}k_+ & 0 \end{pmatrix}, \tag{A2}$$

with $k_\pm = k_x \pm ik_y$ in the basis $\{|\frac{3}{2}, +\frac{3}{2}\rangle, |\frac{3}{2}, -\frac{3}{2}\rangle, |\frac{3}{2}, +\frac{1}{2}\rangle, |\frac{3}{2}, -\frac{1}{2}\rangle\}$ as the HH and LH eigenstates. We can simply use the quasidegenerate perturbation theory to observe the relationship between spin-splitting and the wave vector, by reducing the 4×4 matrix to a 2×2 one. For the first term, the reduced Hamiltonian matrix element $\widetilde{H_{12}}$ keeps zero till the second-order perturbation, and appears to be nonzero at third-order perturbation ($\widetilde{H_{12}} = H'_{13}H'_{34}H'_{42} \propto k_-^3$). Hence the first term gives a cubic splitting $\Delta\varepsilon_{\mathrm{HH}} \propto \beta_1 E_z k_\parallel^3$. For the second term, due to the appearance of nonzero matrix elements $H_{12} = -i\frac{3}{4}k_+$ and $H_{21} = i\frac{3}{4}k_-$, the splitting shows a linear relationship $\Delta\varepsilon_{\mathrm{HH}} \propto \beta_2 E_z k_\parallel$. However, the prefactor β_2, originating from the isotropic $k \cdot p$ coupling between Γ_8^v and Γ_6^c, is much smaller than the prefactor β_1, originating from the anisotropic $k \cdot p$ coupling between Γ_8^v and remote conduction bands Γ_7^c and Γ_8^c [73]. Consequently, the second term could be neglected, even for QWs grown in low-symmetric directions, and the Rashba spin splitting for HH exhibits a **k**-cubic relationship.

TABLE III. Bond-angle parameters of Ge and Si. Here, β, β_3, and β_4 are the bond-angle bending parameters and σ is the parameter of the interaction between bond-length and bond-angle.

Types	σ	β	β_3	β_4
Si-Si-Si	0.74550	13.8273	46.28	373.89
Ge-Ge-Ge	−2.71400	11.3301	57.35	
Ge-Si-Si	−0.98425	12.5787	33.54	186.94
Ge-Si-Ge	−0.98425	12.5787	20.80	
Si-Ge-Ge	−0.98425	12.5787	39.07	
Si-Ge-Si	−0.98425	12.5787	20.80	

TABLE IV. Energies at Γ, X, and L point and effective masses of bulk Ge.

Property	Target value	SEPM value	Error
Γ_{8v} (eV)	0.520	0.522	0.002
Γ_{6c} (eV)	0.90	0.86	−0.04
L_{6c} (eV)	0.74	0.76	0.20
X_{6c} (eV)	1.16	1.13	−0.02
$m^*(\Gamma_{1c})$	0.04	0.40	0.01
$m_l^*(L_{1c})$	1.59	1.47	−0.12
$m_t^*(L_{1c})$	0.08	0.09	0.01
$m_l^*(X_{1c})$	1.59	0.82	−0.77
$m_t^*(X_{1c})$	0.08	0.20	0.12
$m_{hh}^*(100)$	0.20	0.28	0.09
$m_{hh}^*(111)$	0.50	0.73	0.23
$m_{lh}^*(100)$	0.05	0.06	0.01
$m_{lh}^*(111)$	0.04	0.05	0.01
Δ_{SO} (eV)	0.29	0.27	−0.02

However, Eq. (A1) is constructed under the bulk symmetry and the reduction from Eq. (A1) to Eq. (A2) results in a fictitiously higher symmetry for QWs, leading to the ignorance of mixings between pure bulk HH and LH states. In other words, the HH (LH) eigenstates are not pure bulk HH (LH) states, but the so-called HH-type (LH-type) states with the bulk HH (LH) states dominating over the tiny bulk LH (HH) states [Eq. (C4)]. Notably, the second valence bands in QWs can also be of HH-type (see Fig. 2 in the main text), determined by the strength of the space confinement effect (SCE). We next illustrate that the mixings between pure bulk HH and LH states lead to the mixing between the ground states (HH1) and the excited states (HH2), finally resulting in the **k**-linear spin-splitting.

APPENDIX B: SEPM PARAMETERS OF Ge AND Si

We list the SEPM parameters of Ge and Si, including the bond-length parameters and the bond-angle parameters in Tables II and III, respectively. We start the VFF

TABLE V. Energies at Γ, X, and L point and effective masses of bulk Si.

Property	Target value	SEPM value	Error
Γ_{8v} (eV)	0	0	0.00
Γ_{6c} (eV)	3.34	3.36	0.02
L_{6c} (eV)	2.04	2.33	0.29
X_{6c} (eV)	1.13	1.14	0.01
$m^*(\Gamma_{1c})$	0.20	0.40	0.20
$m_l^*(L_{1c})$	1.81	1.72	−0.09
$m_t^*(L_{1c})$	0.12	0.14	0.01
$m_l^*(X_{1c})$	0.92	0.90	−0.01
$m_t^*(X_{1c})$	0.19	0.20	0.01
$m_{hh}^*(100)$	0.34	0.27	−0.07
$m_{hh}^*(111)$	0.69	0.69	0.00
$m_{lh}^*(100)$	0.15	0.21	0.06
$m_{lh}^*(111)$	0.11	0.14	0.03
Δ_{SO} (eV)	0.04	0.04	0.00

TABLE VI. Luttinger parameters for several semiconductors [38].

	GaAs	InAs	InSb	Si	Ge
γ_1	6.85	20.40	37.10	4.28	13.38
γ_2	2.10	8.30	16.50	0.34	4.24
γ_3	2.90	9.10	17.70	1.45	5.69

approach for structure relaxation based on these parameters. We show the SEPM energies at the Γ, X, and L point and effective masses for Ge in Table IV and Si in Table V, respectively.

APPENDIX C: EFFECTIVE 2D HAMILTONIAN OF [001]-ORIENTED QWs

The Luttinger-Kohn (LK) Hamiltonian is commonly used to describe the valence bands. For z along the [001] direction, it is given by [22]

$$H_{\mathrm{LK}}^{[001]} = \frac{\hbar^2}{2m_0}\left[\left(\gamma_1 + \tfrac{5\gamma_2}{2}\right)k^2 - 2\gamma_2\left(k_x^2J_x^2 + k_y^2J_y^2 + k_z^2J_z^2\right) - 4\gamma_3(\{k_x,k_y\}\{J_x,J_y\} + \{k_y,k_z\}\{J_y,J_z\} + \{k_z,k_x\}\{J_z,J_x\})\right]. \quad \text{(C1)}$$

Here the x and y directions are along the crystallographic [100] and [010] directions, respectively. And γ_1, γ_2, and γ_3 are the LK parameters with the values shown in Table VI [38]. Next, we express the $H_{\mathrm{LK}}^{[001]}$ in the basis $\{|+\tfrac{3}{2}\rangle, |-\tfrac{3}{2}\rangle, |+\tfrac{1}{2}\rangle, |-\tfrac{1}{2}\rangle\}$ as

$$H_{\mathrm{eff}}^{[001]}(k_\pm,k_z) = \begin{pmatrix} \mu(\frac{\gamma_1+\gamma_2}{2}k_\parallel^2 + \frac{\gamma_1-2\gamma_2}{2}k_z^2) & 0 & -\sqrt{3}\mu\gamma_3k_-k_z & -\frac{\sqrt{3}\mu}{2}(\eta k_-^2 + \delta k_+^2) \\ 0 & \mu(\frac{\gamma_1+\gamma_2}{2}k_\parallel^2 + \frac{\gamma_1-2\gamma_2}{2}k_z^2) & -\frac{\sqrt{3}\mu}{2}(\eta k_+^2 + \delta k_-^2) & \sqrt{3}\mu\gamma_3k_+k_z \\ -\sqrt{3}\mu\gamma_3k_+k_z & -\frac{\sqrt{3}\mu}{2}(\eta k_-^2 + \delta k_+^2) & \mu(\frac{\gamma_1-\gamma_2}{2}k_\parallel^2 + \frac{\gamma_1+2\gamma_2}{2}k_z^2) & 0 \\ -\frac{\sqrt{3}\mu}{2}(\eta k_+^2 + \delta k_-^2) & \sqrt{3}\mu\gamma_3k_-k_z & 0 & \mu(\frac{\gamma_1-\gamma_2}{2}k_\parallel^2 + \frac{\gamma_1+2\gamma_2}{2}k_z^2) \end{pmatrix}, \quad \text{(C2)}$$

where $\mu = \frac{\hbar^2}{m_0}$, $\eta = \frac{\gamma_2+\gamma_3}{2}$, $\delta = \frac{\gamma_2-\gamma_3}{2}$, $k_\pm = k_x \pm ik_y$, and $k_\parallel = \sqrt{k_x^2+k_y^2}$. Considering the confinement ($-L/2 < z < L/2$) as a hard wall, we can describe the envelope function using

$$\phi_n(z) = \sqrt{\frac{2}{L}}\sin[\frac{n\pi(z+L/2)}{L}]. \quad \text{(C3)}$$

In the presence of HH-LH mixing, the four basis states read

$$\begin{aligned} |\mathrm{HH1}_\pm\rangle &= a_1\phi_1(z)\left|\frac{3}{2},\pm\frac{3}{2}\right\rangle + b_1\phi_1(z)\left|\frac{3}{2},\mp\frac{1}{2}\right\rangle, \\ |\mathrm{HH2}_\pm\rangle &= a_2\phi_2(z)\left|\frac{3}{2},\pm\frac{3}{2}\right\rangle + b_2\phi_2(z)\left|\frac{3}{2},\mp\frac{1}{2}\right\rangle. \end{aligned} \quad \text{(C4)}$$

Here, $|\mathrm{HH1}_\pm\rangle$ and $|\mathrm{HH2}_\pm\rangle$ denote the ground states (HH1) and the first excited states (HH2), respectively, with the subscripts "+" and "−" representing two different "spin blocks" of the contained spin states $|3/2, \pm 3/2\rangle$ at the $\bar{\Gamma}$ point. Then, we obtain the effective 2D Hamiltonian in the presence of perpendicular external electric field written as

$$H_{\mathrm{eff}}^{[001]} = \begin{pmatrix} \frac{\hbar^2k_x^2}{2m_{1x}} + \frac{\hbar^2k_y^2}{2m_{1y}} & 0 & eU_0E_z & -i\gamma_3C_0k_- \\ 0 & \frac{\hbar^2k_x^2}{2m_{1x}} + \frac{\hbar^2k_y^2}{2m_{1y}} & i\gamma_3C_0k_+ & eU_0E_z \\ eU_0E_z & -i\gamma_3C_0k_- & \frac{\hbar^2k_x^2}{2m_{2x}} + \frac{\hbar^2k_y^2}{2m_{2y}} + \Delta_0 & 0 \\ i\gamma_3C_0k_+ & eU_0E_z & 0 & \frac{\hbar^2k_x^2}{2m_{2x}} + \frac{\hbar^2k_y^2}{2m_{2y}} + \Delta_0 \end{pmatrix}, \quad \text{(C5)}$$

where $U_0 = (a_1a_2 + b_1b_2)\frac{16L}{9\pi^2}$ denotes the direct coupling strength to the external electric field, $C_0 = (a_1b_2 - a_2b_1)\frac{8\sqrt{3}\mu}{3L}$ characterizes the mixing strength between the HH-type ground states and the HH-type excited states, and Δ_0 is the energy separation between HH1 and HH2 states.

Next, we use the quasidegenerate perturbation theory to reduce this 4×4 effective Hamiltonian and obtain the **k**-linear direct Rashba parameter. Analogous to the derivation in Ref. [21], the reduction of this Hamiltonian involves three steps. First, we split it into two parts, including the leading-order part and the perturbation part. Then we find a unitary matrix to diagonalize the

leading-order Hamiltonian and obtain the transformed perturbation Hamiltonian. Finally, we use the standard quasidegenerate perturbation theory to obtain the reduced effective Hamiltonian.

In the first step, considering the wave vector near the Brillion zone center, we split the 4×4 effective Hamiltonian $H^{\text{eff}}_{4\times4}$ [Eq. (C5)] into the leading-order Hamiltonian

$$H^0_{4\times4} = \begin{pmatrix} 0 & 0 & eU_0E_z & 0 \\ 0 & 0 & 0 & eU_0E_z \\ eU_0E_z & 0 & \Delta_0 & 0 \\ 0 & eU_0E_z & 0 & \Delta_0 \end{pmatrix}, \tag{C6}$$

and the perturbation Hamiltonian

$$H'_{4\times4} = \begin{pmatrix} \frac{\hbar^2k_x^2}{2m_{1x}} + \frac{\hbar^2k_y^2}{2m_{1y}} & 0 & 0 & -i\gamma_3C_0k_- \\ 0 & \frac{\hbar^2k_x^2}{2m_{1x}} + \frac{\hbar^2k_y^2}{2m_{1y}} & i\gamma_3C_0k_+ & 0 \\ 0 & -i\gamma_3C_0k_- & \frac{\hbar^2k_x^2}{2m_{2x}} + \frac{\hbar^2k_y^2}{2m_{2y}} & 0 \\ i\gamma_3C_0k_+ & 0 & 0 & \frac{\hbar^2k_x^2}{2m_{2x}} + \frac{\hbar^2k_y^2}{2m_{2y}} \end{pmatrix}. \tag{C7}$$

All the elements in the leading-order Hamiltonian $H^0_{4\times4}$ are eU_0E_z or Δ_0, and all **k**-linear and **k**-squared terms are involved in the perturbation Hamiltonian $H'_{4\times4}$.

In the second step, we use the unitary matrix $\tilde{U}$ to perform the unitary transformation $\tilde{U}^\dagger H^{\text{eff}}_{4\times4}\tilde{U}$. The unitary matrix can be written as

$$\tilde{U} = \begin{pmatrix} \cos\theta & 0 & \sin\theta & 0 \\ 0 & -\cos\theta & 0 & \sin\theta \\ -\sin\theta & 0 & \cos\theta & 0 \\ 0 & \sin\theta & 0 & \cos\theta \end{pmatrix}, \tag{C8}$$

where

$$\begin{aligned} \cos\theta &= \frac{\Delta_0 + \Delta'}{\sqrt{(\Delta_0 + \Delta')^2 + (2eU_0E_z)^2}}, \\ \sin\theta &= \frac{2eU_0E_z}{\sqrt{(\Delta_0 + \Delta')^2 + (2eU_0E_z)^2}}, \end{aligned} \tag{C9}$$

with

$$\Delta' = \sqrt{\Delta_0^2 + (2eU_0E_z)^2}. \tag{C10}$$

We then obtain the transformed leading-order Hamiltonian [omitting the constant energy shift $(\Delta_0 - \Delta')/2$]

$$\tilde{H}^{(0)}_{4\times4} = \tilde{U}^\dagger H^0_{4\times4}\tilde{U} = \begin{pmatrix} 0 & 0 & 0 & 0 \\ 0 & 0 & 0 & 0 \\ 0 & 0 & \Delta' & 0 \\ 0 & 0 & 0 & \Delta' \end{pmatrix}, \tag{C11}$$

and the transformed perturbation Hamiltonian

$$\tilde{H}'_{4\times4} = \tilde{U}^\dagger H'_{4\times4}\tilde{U} = \begin{pmatrix} E_1 & -i\gamma_3C_0k_-\sin2\theta & T & -i\gamma_3C_0k_-\cos2\theta \\ i\gamma_3C_0k_+\sin2\theta & E_1 & i\gamma_3C_0k_+\cos2\theta & -T \\ T & -i\gamma_3C_0k_-\cos2\theta & E_2 & -i\gamma_3C_0k_-\sin2\theta \\ i\gamma_3C_0k_+\cos2\theta & -T & i\gamma_3C_0k_+\sin2\theta & E_2 \end{pmatrix}, \tag{C12}$$

where

$$\begin{aligned} E_1 &= \left(\frac{\hbar^2k_x^2}{2m_{1x}} + \frac{\hbar^2k_y^2}{2m_{1y}}\right)\cos^2\theta + \left(\frac{\hbar^2k_x^2}{2m_{2x}} + \frac{\hbar^2k_y^2}{2m_{2y}}\right)\sin^2\theta, \\ E_2 &= \left(\frac{\hbar^2k_x^2}{2m_{1x}} + \frac{\hbar^2k_y^2}{2m_{1y}}\right)\sin^2\theta + \left(\frac{\hbar^2k_x^2}{2m_{2x}} + \frac{\hbar^2k_y^2}{2m_{2y}}\right)\cos^2\theta, \\ T &= \left[\left(\frac{\hbar^2k_x^2}{4m_{1x}} + \frac{\hbar^2k_y^2}{4m_{1y}}\right) - \left(\frac{\hbar^2k_x^2}{4m_{2x}} + \frac{\hbar^2k_y^2}{4m_{2y}}\right)\right]\sin2\theta. \end{aligned} \tag{C13}$$

In the third step, we use the standard second-order quasidegenerate theory to obtain the reduced 2×2 effective Hamiltonian

$$H_{2\times2}^{\text{eff}} = \left[\left(\frac{\hbar^2k_x^2}{4m_{1x}} + \frac{\hbar^2k_y^2}{4m_{1y}}\right) + \left(\frac{\hbar^2k_x^2}{4m_{2x}} + \frac{\hbar^2k_y^2}{4m_{2y}}\right)\right] + \frac{\Delta_0}{\Delta'}\left[\left(\frac{\hbar^2k_x^2}{4m_{1x}} + \frac{\hbar^2k_y^2}{4m_{1y}}\right) - \left(\frac{\hbar^2k_x^2}{4m_{2x}} + \frac{\hbar^2k_y^2}{4m_{2y}}\right)\right] - \frac{\Delta_0^2\gamma_3^2C_0^2(k_x^2+k_y^2)}{(\Delta')^3} + \frac{2e\gamma_3C_0U_0E_z}{\Delta'}(k_x\sigma_y - k_y\sigma_x). \tag{C14}$$

We illustrate that only the fourth term in Eq. (C14) is the first-order result, and the other terms are the second-order results. Obviously, for the **k**-linear terms, the first-order perturbation provides sufficiently reliable **k**-linear results. Consequently, the direct Rashba parameter has the form

$$\alpha_R = \frac{2e\gamma_3C_0U_0E_z}{\sqrt{\Delta_0^2 + 4e^2U_0^2E_z^2}}, \tag{C15}$$

given by the first-order coupling to the external electric field. If the eigenstates were pure HH states ($b_1 = b_2 = 0$), we would obtain $C_0 = 0$ and $U_0 = 0$, and thus $\alpha_R = 0$. This implies that the lack of HH-LH mixing at the zone center will lead to the vanishment of the **k**-linear Rashba SOC. Although the proposed effective model is phenomenological by assuming the infinite confinement potential, this model succeeds in describing the origin and change of the **k**-linear Rashba SOC in 2DHGs.

APPENDIX D: EFFECTIVE 2D HAMILTONIAN OF [110]-ORIENTED QWs

For the [110] direction, the LK Hamiltonian reads [22]

$$\begin{aligned} H_{\text{LK}}^{[110]} =& \frac{\hbar^2}{2m_0}[(\gamma_1 + \frac{5\gamma_2}{2})k^2 - \gamma_2(2k_x^2J_x^2 + k_y^2J_y^2 + k_z^2J_z^2) \\ & - \gamma_2(k_y^2J_z^2 + k_z^2J_y^2 + 4\{k_y, k_z\}\{J_y, J_z\}) \\ & - 4\gamma_3(\{k_x, k_y\}\{J_x, J_y\} + \{k_z, k_x\}\{J_z, J_x\}) \\ & - \gamma_3(k_y^2 - k_z^2)(J_y^2 - J_z^2)]. \end{aligned} \tag{D1}$$

Here the x and y directions are along the crystallographic [001] and [1$\bar{1}$0] directions, respectively. In the basis $\{|\frac{3}{2}, +\frac{3}{2}\rangle, |\frac{3}{2}, -\frac{3}{2}\rangle, |\frac{3}{2}, +\frac{1}{2}\rangle, |\frac{3}{2}, -\frac{1}{2}\rangle\}$, the $H_{\text{LK}}^{[110]}(k_\pm, k_z)$ is written as

$$H_{\text{eff}}^{[110]}(\mathbf{k}) = \frac{\mu}{2}\begin{pmatrix} M_1 & 0 & 2\sqrt{3}k_z(-\gamma_3k_x + i\gamma_2k_y) & T_1 + \sqrt{3}\delta k_z^2 \\ 0 & M_1 & T_1^\dagger + \sqrt{3}\delta k_z^2 & 2\sqrt{3}k_z(\gamma_3k_x + i\gamma_2k_y) \\ 2\sqrt{3}k_z(-\gamma_3k_x - i\gamma_2k_y) & T_1 + \sqrt{3}\delta k_z^2 & M_2 & 0 \\ T_1^\dagger + \sqrt{3}\delta k_z^2 & 2\sqrt{3}k_z(\gamma_3k_x - i\gamma_2k_y) & 0 & M_2 \end{pmatrix}, \tag{D2}$$

with $\mu = \frac{\hbar^2}{m_0}$, $T_1 = \gamma_2(\frac{\sqrt{3}k_y^2}{2} - \sqrt{3}k_x^2) + 2i\sqrt{3}\gamma_3k_xk_y + \frac{1}{2}\sqrt{3}\gamma_3k_y^2$, $M_1 = -\frac{3}{2}[\gamma_2k_x^2 + (2\gamma_2 - \gamma_3)k_y^2 + (2\gamma_2 + \gamma_3)k_z^2]$, and $M_2 = -\frac{7}{2}\gamma_2k_x^2 - (2\gamma_2 + \frac{3}{2}\gamma_3)k_y^2 + (\frac{3}{2}\gamma_3 - 2\gamma_2)k_z^2$. By assuming $k_x = k_y = 0$, one can see that there is an intrinsic mixing of HH and LH, which is proportional to $\delta \times k_z^2$.

Similarly, we construct the basis states in the presence of HH-LH mixing as that of [001]-oriented QW in Eq. (C4) and obtain the effective 2D Hamiltonian under the perpendicular external electric field for [110]-oriented QWs

$$H_{\text{eff}}^{[110]} = \begin{pmatrix} \frac{\gamma_3^2\hbar^2k_x^2}{2m_{1x}} + \frac{\gamma_2^2\hbar^2k_y^2}{2m_{1y}} & 0 & eU_0E_z & -iC_0(\gamma_3k_x - i\gamma_2k_y) \\ 0 & \frac{\gamma_3^2\hbar^2k_x^2}{2m_{1x}} + \frac{\gamma_2^2\hbar^2k_y^2}{2m_{1y}} & iC_0(\gamma_3k_x + i\gamma_2k_y) & eU_0E_z \\ eU_0E_z & -iC_0(\gamma_3k_x - i\gamma_2k_y) & \frac{\gamma_3^2\hbar^2k_x^2}{2m_{2x}} + \frac{\gamma_2^2\hbar^2k_y^2}{2m_{2y}} + \Delta_0 & 0 \\ iC_0(\gamma_3k_x + i\gamma_2k_y) & eU_0E_z & 0 & \frac{\gamma_3^2\hbar^2k_x^2}{2m_{2x}} + \frac{\gamma_2^2\hbar^2k_y^2}{2m_{2y}} + \Delta_0 \end{pmatrix}. \tag{D3}$$

Finally, using the quasidegenerate perturbation theory (similar to the derivation of [001]-oriented QWs), we obtain the **k**-linear direct Rashba splitting term, which takes the form of $\alpha_R^{[110]} = \frac{2e\gamma_3C_0U_0E_z}{\sqrt{\Delta_0{}^2+4e^2U_0{}^2E_z^2}}$ for k_x and $\alpha_R^{[110]} = \frac{2e\gamma_2C_0U_0E_z}{\sqrt{\Delta_0{}^2+4e^2U_0{}^2E_z^2}}$ for k_y.

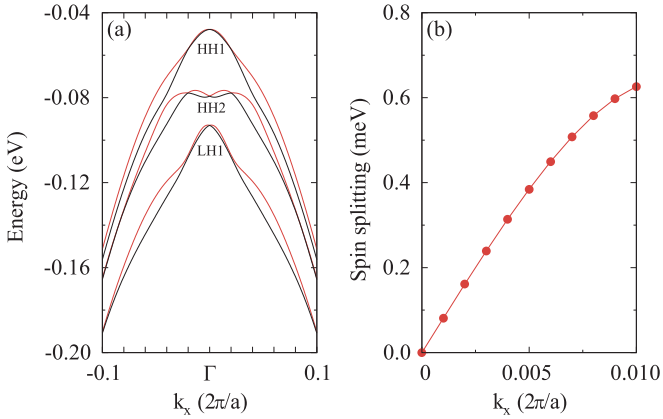

FIG. 6. (a) Calculated energy dispersion of valence subbands and (b) spin splitting of HH1 for [110]-oriented $(GaAs)_{20}/(AlAs)_{20}$ QWs. The external perpendicular electric field is $E_z = 100$ kV/cm. The x-direction is along the crystalline [001] direction. The labels HH1, HH2, LH1 in (a) represent the main components of each Kramers pair of valence subband states at Γ point, respectively.

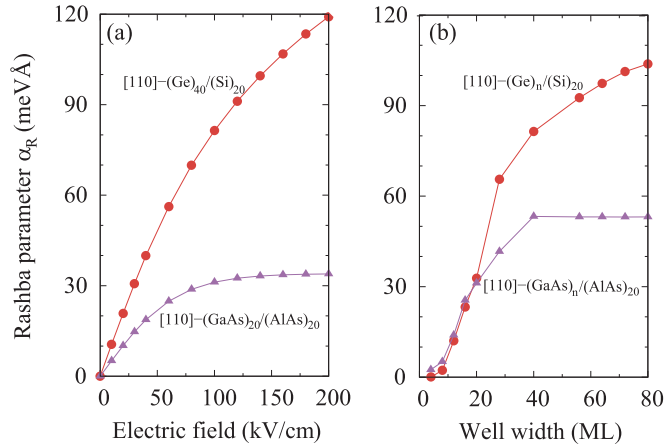

FIG. 7. Calculated **k**-linear hole Rashba parameters α_R along the k_x direction in [110]-oriented GaAs/AlAs QWs and [110]-oriented Ge/Si QWs as a function of (a) electric field strength with fixed well thickness and (b) well thickness under an electric field of 100 kV/cm, respectively. (For GaAs/AlAs QWs, the number of the subscript denotes the number of bilayers.) Note that a larger electric field strength than 200 kV/cm is not experimentally available, hence the results are not shown.

APPENDIX E: RESULTS OF [110]-ORIENTED GaAs/AlAs QWs

The **k**-linear Rashba SOC also exists in GaAs/AlAs QWs. As shown in Fig. 6, the Rashba spin splitting of [110]-oriented $GaAs_{20}/AlAs_{20}$ QWs exhibits a **k**-linear relationship as well, where the Rashba parameter reaches the value of 31 meVÅ. Figure 7 shows the relationship between **k**-linear Rashba parameters and electric field and well thickness, comparing the parameters of [110]-oriented GaAs/AlAs QWs and [110]-oriented Ge/Si QWs.

[1] S. Datta and B. Das, Appl. Phys. Lett. **56**, 665 (1990).
[2] J. Schliemann, J. C. Egues, and D. Loss, Phys. Rev. Lett. **90**, 146801 (2003).
[3] R. Maurand, X. Jehl, D. Kotekar-Patil, A. Corna, H. Bohuslavskyi, R. Lavieville, L. Hutin, S. Barraud, M. Vinet, M. Sanquer, and S. De Franceschi, Nat. Commun. **7**, 13575 (2016).
[4] H. Watzinger, J. Kukucka, L. Vukusic, F. Gao, T. Wang, F. Schaffler, J.-J. Zhang, and G. Katsaros, Nat. Commun. **9**, 3902 (2018).
[5] J. Sinova, D. Culcer, Q. Niu, N. A. Sinitsyn, T. Jungwirth, and A. H. MacDonald, Phys. Rev. Lett. **92**, 126603 (2004).
[6] D. Xiao, M. C. Chang, and Q. Niu, Rev. Mod. Phys. **82**, 1959 (2010).
[7] B. A. Bernevig and S.-C. Zhang, Phys. Rev. Lett. **95**, 016801 (2005).
[8] B. A. Bernevig, T. L. Hughes, and S. C. Zhang, Science **314**, 1757 (2006).
[9] D. D. Awschalom, L. C. Bassett, A. S. Dzurak, E. L. Hu, and J. R. Petta, Science **339**, 1174 (2013).
[10] R. M. Lutchyn, J. D. Sau, and S. Das Sarma, Phys. Rev. Lett. **105**, 077001 (2010).
[11] V. Mourik, K. Zuo, S. M. Frolov, S. R. Plissard, and L. P. Kouwenhoven, Science **336**, 1003 (2012).
[12] A. Manchon, H. C. Koo, J. Nitta, S. M. Frolov, and R. A. Duine, Nat. Mater. **14**, 871 (2015).
[13] N. W. Hendrickx, D. P. Franke, A. Sammak, G. Scappucci, and M. Veldhorst, Nature **577**, 487 (2020).
[14] M. Failla, J. Keller, G. Scalari, C. Maissen, J. Faist, C. Reichl, W. Wegscheider, O. J. Newell, D. R. Leadley, and M. Myronov, New J. Phys. **18**, 113036 (2016).
[15] R. Winkler, *Spin-Orbit Coupling Effect in Two-Dimensional Electron and Hole Systems* (Springer, New York, 2003).
[16] D. V. Bulaev and D. Loss, Phys. Rev. Lett. **95**, 076805 (2005).
[17] D. V. Bulaev and D. Loss, Phys. Rev. Lett. **98**, 097202 (2007).
[18] M. G. Pala, M. Governale, J. Konig, U. Zulicke, and G. Lannaccone, Phys. Rev. B **69**, 045304 (2004).
[19] R. Moriya, K. Sawano, Y. Hoshi, S. Masubuchi, Y. Shiraki, A. Wild, C. Neumann, G. Abstreiter, D. Bougeard, T. Koga, and T. Machida, Phys. Rev. Lett. **113**, 086601 (2014).
[20] J.-W. Luo, L. Zhang, and A. Zunger, Phys. Rev. B **84**, 121303(R) (2011).
[21] C. Kloeffel, M. Trif, and D. Loss, Phys. Rev. B **84**, 195314 (2011).
[22] C. Kloeffel, M. J. Rančić, and D. Loss, Phys. Rev. B **97**, 235422 (2018).
[23] J.-W. Luo, S.-S. Li, and A. Zunger, Phys. Rev. Lett. **119**, 126401 (2017).
[24] J.-W. Luo, A. N. Chantis, M. van Schilfgaarde, G. Bester, and A. Zunger, Phys. Rev. Lett. **104**, 066405 (2010).
[25] J.-W. Luo, G. Bester, and A. Zunger, Phys. Rev. B **92**, 165301 (2015).
[26] E. L. Ivchenko, A. Y. Kaminski, and U. Rössler, Phys. Rev. B **54**, 5852 (1996).
[27] O. Krebs and P. Voisin, Phys. Rev. Lett. **77**, 1829 (1996).

[28] A. A. Toropov, E. L. Ivchenko, O. Krebs, S. Cortez, P. Voisin, and J. L. Gentner, Phys. Rev. B **63**, 035302 (2000).
[29] M. V. Durnev, M. M. Glazov, and E. L. Ivchenko, Phys. Rev. B **89**, 075430 (2014).
[30] E. I. Rashba and E. Y. Sherman, Phys. Lett. A **129**, 175 (1988).
[31] J. Schliemann and D. Loss, Phys. Rev. B **69**, 165315 (2004).
[32] N. Sugimoto, S. Onoda, S. Murakami, and N. Nagaosa, Phys. Rev. B **73**, 113305 (2006).
[33] A. Wong and F. Mireles, Phys. Rev. B **81**, 085304 (2010).
[34] X. Bi, P. He, E. M. Hankiewicz, R. Winkler, G. Vignale, and D. Culcer, Phys. Rev. B **88**, 035316 (2013).
[35] S. D. Ganichev, E. L. Ivchenko, V. V. Bel'kov, S. A. Tarasenko, M. Sollinger, D. Weiss, W. Wegscheider, and W. Prettl, Nature **417**, 153 (2002).
[36] V. E. Sacksteder and B. A. Bernevig, Phys. Rev. B **89**, 161307(R) (2014).
[37] C.-X. Liu, B. Zhou, S.-Q. Shen, and B.-F. Zhu, Phys. Rev. B **77**, 125345 (2008).
[38] E. Marcellina, A. R. Hamilton, R. Winkler, and D. Culcer, Phys. Rev. B **95**, 075305 (2017).
[39] L.-W. Wang and A. Zunger, J. Chem. Phys. **100**, 2394 (1994).
[40] L.-W. Wang and A. Zunger, Phys. Rev. B **51**, 17398 (1995).
[41] L.-W. Wang, J. Kim, and A. Zunger, Phys. Rev. B **59**, 5678 (1999).
[42] P. Y. Yu and M. Cardona, *Fundamentals of Semiconductors Physics and Materials Properties* (Springer, New York, 2005).
[43] A. J. Williamson, L.-W. Wang, and A. Zunger, Phys. Rev. B **62**, 12963 (2000).
[44] C. Pryor, J. Kim, L.-W. Wang, A. J. Williamson, and A. Zunger, J. Appl. Phys. **83**, 2548 (1998).
[45] J.-W. Luo, S.-S. Li, J.-B. Xia, and L.-W. Wang, Phys. Rev. B **71**, 245315 (2005).
[46] M. d'Avezac, J.-W. Luo, T. Chanier, and A. Zunger, Phys. Rev. Lett. **108**, 027401 (2012).
[47] L.-J. Zhang, M. d'Avezac, J.-W. Luo, and A. Zunger, Nano Lett. **12**, 984 (2012).
[48] L.-J. Zhang, J.-W. Luo, A. Saraiva, B. Koiller, and A. Zunger, Nat. Commun. **4**, 2396 (2013).
[49] J.-W. Luo, G. Bester, and A. Zunger, Phys. Rev. Lett. **102**, 056405 (2009).
[50] J.-W. Luo and A. Zunger, Phys. Rev. Lett. **105**, 176805 (2010).
[51] J.-W. Luo, S.-S. Li, I. Sychugov, F. Pevere, J. Linnros, and A. Zunger, Nat. Nanotech. **12**, 930 (2017).
[52] G. Dresselhaus, Phys. Rev. **100**, 580 (1955).
[53] Y. A. Bychkov and E. I. Rashba, JETP Lett. **39**, 78 (1984).
[54] J. M. Luttinger, Phys. Rev. **102**, 1030 (1956).
[55] J. R. Schrieffer and P. A. Wolff, Phys. Rev. **149**, 491 (1966).
[56] N. S. Averkiev and L. E. Golub, Phys. Rev. B **60**, 15582 (1999).
[57] J. Wunderlich, B.-G. Park, A. C. Irvine, L. P. Zârbo, E. Rozkotová, P. Nemec, V. Novák, J. Sinova, and T. Jungwirth, Science **330**, 1801 (2010).
[58] J. D. Koralek, C. P. Weber, J. Orenstein, B. A. Bernevig, S.-C. Zhang, S. Mark, and D. D. Awschalom, Nature **458**, 610 (2009).
[59] J. Wunderlich, A. C. Irvine, J. Sinova, B. G. Park, L. P. Zarbo, X. L. Xu, B. Kaestner, V. Novak, and T. Jungwirth, Nat. Phys. **5**, 675 (2009).
[60] E. L. Ivchenko and G. E. Pikus, JETP Lett. **27**, 604 (1978).
[61] S. D. Ganichev, Int. J. Mod. Phys. B **22**, 1 (2008).
[62] C. Morrison and M. Myronov, Appl. Phys. Lett. **111**, 192103 (2017).
[63] M. Lodari, A. Tosato, D. Sabbagh, M. A. Schubert, G. Capellini, A. Sammak, M. Veldhorst, and G. Scappucci, Phys. Rev. B **100**, 041304(R) (2019).
[64] E. Gatti, F. Isa, D. Chrastina, E. M. Gubler, F. Pezzoli, E. Grilli, and G. Isella, J. Appl. Phys. **116**, 043518 (2014).
[65] C. Yang and D. Pan, J. Appl. Phys. **64**, 1573 (1988).
[66] C. Lee and K. L. Wang, Appl. Phys. Lett. **60**, 2264 (1992).
[67] C. W. Liu, J. C. Sturm, Y. R. J. Lacroix, M. L. W. Thewalt, and D. D. Perovic, Appl. Phys. Lett. **65**, 76 (1994).
[68] P. E. Thompson, D. Godbey, K. Hobart, E. Glaser, and T. Kennedy, Jpn. J. Appl. Phys. **33**, 2317 (1994).
[69] T. L. Kreifels, R. L. Hengehold, Y. K. Yeo, P. E. Thompson, and D. S. Simons, J. Vaccum Sci. Technol. A **13**, 636 (1995).
[70] P. E. Thompson, T. L. Kreifels, M. Gregg, R. L. Hengehold, Y. K. Yeo, D. S. Simons, M. E. Twigg, M. Fatemi, and K. Hobart, J. Cryst. Growth **157**, 21 (1995).
[71] S. Dissanayake, Y. Zhao, S. Sugahara, M. Takenaka, and S. Takagi, J. Appl. Phys. **109**, 033709 (2011).
[72] V. H. Nguyen, A. Dobbie, M. Myronov, and D. R. Leadley, J. Appl. Phys. **114**, 154306 (2013).
[73] R. Winkler, Phys. Rev. B **62**, 4245 (2000).